Check for updates

ADVANCED OPTICAL MATERIALS
www.advopticalmat.de

Terahertz Plasmon Polaritons in Large Area Bi_2Se_3 Topological Insulators

*Valentino Pistore, Leonardo Viti, Chiara Schiattarella, Elisa Riccardi, Craig S. Knox, Ahmet Yagmur, Joel J. Burton, Satoshi Sasaki, A. Giles Davies, Edmund H. Linfield, Joshua R. Freeman, and Miriam S. Vitiello**

Assessing the nature of topological quantum materials, and in particular probing the existence of topological surface states, is a very challenging task. Terahertz (THz) frequency scattering near-field optical microscopy has emerged as an effective technique to investigate the presence of massless surface carriers by locally probing collective surface excitations, i.e., plasmon polaritons, whose dispersion critically depends on the density and nature of surface carriers. Here, thin (14–19 nm) films of Bi_2Se_3 are experimentally investigated through a combination of x-ray diffraction, Hall-bar magneto-transport, and near-field detectorless optical holography at THz frequencies, from 2 to 4.3 THz. The dispersion of surface plasmon polaritons are determined for different Bi_2Se_3 film thicknesses, proving the presence of massless surface carriers. The results open intriguing opportunities in THz nano-plasmonics and topological nano-photonics including the development of superlenses and metasurfaces, making use of plasmon polaritons.

1. Introduction

Topological insulators (TIs) are materials that exhibit an insulating behavior in the bulk, accompanied by gapless edge or surface states at the boundaries,[1] conventionally called topological surface states (TSSs). TSSs have a linear dispersion, forming a Dirac cone around the Γ point of the Brillouin zone, and are maintained even in the presence of surface defects and disorder.[2]

In commonly studied three-dimensional TIs, such as Bi_2Se_3 and Bi_2Te_3, the strong spin-orbit interaction results in an inverted bulk band gap, requiring the existence of topologically protected bands at the TI-vacuum and TI-substrate interfaces.[3,4] Owing to this, Dirac electrons in a TSS show spin-momentum locking and suppressed back-scattering.[1] As a result of the dissipation-free transport occurring within the TSSs,[5] TIs can enable the development of new technologies, paving the way to low-power electronics applications, spanning from thermoelectrics to magnetic memories.[6,7]

Key requirements for widespread adoption of TIs and for room-temperature application in future electronic and photonic devices include the ability to achieve high-quality samples with well-defined interfaces and, importantly, the development of industrial-scale and inexpensive production processes. This has led to theoretical[8–11] and experimental efforts to synthesize,[12] characterize,[13–15] and optimize[16] the properties of this novel state of matter. Recently, bismuth-based TI materials, such as Bi_2Se_3 and Bi_2Te_3, have been object of significant improvements in their synthesis techniques,[12,17] study of materials properties,[18] and in-depth characterization of their TSSs.[19] A wide range of experimental techniques have been used to study this class of TI materials, including magneto-transport measurements,[20,21] angle-resolved photo-emission spectroscopy (ARPES),[22,23] scanning tunneling microscopy (STM),[24,25] and optical conductivity.[26,27] ARPES provides the most direct measurement of the dispersion of surface states, and is the most commonly adopted approach to directly assess the electronic band dispersion of a TI.[5,28] However, ARPES requires pristine surfaces, difficult to be preserved in TI-devices.

Interestingly, TIs based on bismuth compounds possess phonon spectra with characteristic features at terahertz (THz) frequencies (≈2–3 THz, 8–12 meV), which makes them ideal as nonlinear materials for the investigation of new

---

V. Pistore, L. Viti, C. Schiattarella, E. Riccardi, M. S. Vitiello
NEST
CNR-Istituto Nanoscienze and Scuola Normale Superiore
Piazza San Silvestro 12, Pisa 56127, Italy
E-mail: miriam.vitiello@sns.it

C. S. Knox, A. G. Davies, E. H. Linfield, J. R. Freeman
School of Electronic and Electrical Engineering
University of Leeds
Leeds LS2 9JT, UK

A. Yagmur, J. J. Burton, S. Sasaki
School of Physics and Astronomy
University of Leeds
Leeds LS2 9JT, UK

The ORCID identification number(s) for the author(s) of this article can be found under https://doi.org/10.1002/adom.202301673

DOI: 10.1002/adom.202301673

phenomena such as high-order non-linear generation in unexplored frequency regions.[29] Strong light-matter interaction in the far-infrared has also drawn significant attention to the optical properties of Bi_2Se_3, which have been extensively characterized by Fourier-transform infrared (FTIR) and time-domain spectroscopies. These have demonstrated the presence of massless carriers at the TI surface,[14] although the relative contribution of surface and bulk states is still a subject of debate, as well as the possibility of exciting ultrafast surface shift currents.[30]

Traditionally, TI films have been grown through three main techniques: the Volmer-Weber approach,[31] where deposited atoms nucleate in separate islands that merge into continuous thin films; the Frank-Van der Merwe (layer) technique,[31] where crystals grow layer-by-layer and atoms are attached to the substrate by surface adhesive force; the Stranski-Krastanov (SK) growth mode,[32] where layers form first and then the system switches to island growth. Single crystalline ingots of Bi_2Se_3 can be also grown from melt by the vertical Bridgman-Stockbarger method.[33,34] The final grown material consists of one large single crystalline block, from which the corresponding TIs can be mechanically exfoliated.[35] Alternative methods include sonochemical synthesis,[36] metal-organic chemical vapor deposition (MOCVD),[37] and chemical vapor deposition (CVD).[38] The most sophisticated and systematic way to grow large-area and scalable TI materials is by molecular beam epitaxy (MBE), which has recently emerged as a means of growing Bi_2Se_3 films of controlled thickness and thin film heterostructures with controlled composition.[39,40]

Here, we perform a detailed experimental investigation of MBE-grown Bi_2Se_3 films by x-ray diffraction and Hall-bar magneto-transport measurements to assess sheet carrier density, Hall mobility, and sheet resistance. This is correlated with micro-Raman spectroscopy and scattering-type scanning near-field optical microscopy (s-SNOM) and optical holography (OH)[41] at THz frequencies to probe the optical response of the samples and to reconstruct the dispersion of collective excitation (surface plasmon polaritons – SPP) in the material. Through the comparison between magneto-transport results, data extrapolated via s-SNOM and those predicted theoretically, we prove the topological nature of the investigated material and quantify the relative contributions of the different carrier contributing to their dispersion curve.

1.1. Sample growth, X-ray diffraction, and Raman characterization

Two different TI samples were grown on [0001] sapphire substrates, following the procedure detailed in ref. [42] Samples A and B are Bi_2Se_3 grown with Bi:Se flux ratios 1:40 and 1:30, respectively. Samples were removed from the chamber, diced and the structural properties analyzed by x-ray reflectivity and diffraction, using Cu-Kα radiation. Other areas of the sample were subsequently mounted for 4- and 6-probe transport measurements before being loaded into a continuous-flow He cryostat with a base temperature of 1.6 K and an 8 T superconducting magnet. Transverse and longitudinal conductivities were measured using lock-in amplifier techniques at a frequency of 119.77 Hz, at the base temperature of the cryostat.

The ($\omega-2\theta$) x-ray reflectivity scans are shown in **Figure 1**a. All samples show Pendellosung fringes[43] surrounding the [0003] x-ray diffraction peak, indicative of strong vertical ordering. The two samples share the *c*-axis lattice parameter of 2.86 ± 0.01 nm, in good agreement with the bulk lattice parameter of Bi_2Se_3, 2.863 nm.[44] This result implies that the crystal structure of the TI films is relaxed and well ordered, despite the large lattice mismatch to the sapphire substrate.

We transferred both the 14.4 nm (sample A) and the 19.0 nm (sample B) Bi_2Se_3 thin films onto a SiO_2/Si host wafer to prevent absorption at high frequencies from the sapphire growth substrate. In order to assess the crystal quality after transfer, we performed Raman characterization of samples A and B, as shown in Figures 1b,c, respectively. Micro-Raman spectra (Horiba, ExploraPlus microscope) were measured using a 532 nm, 1 μW, CW pump laser focused over a spot of radius ≈2 μm. Owing to the low thermal conductivity of Bi_2Se_3,[45] we selected a low-power excitation to exclude laser heating effects on the Raman spectra. Three prominent vibrational modes[46] characteristic of Bi_2Se_3 were observed, corresponding to the out-of-plane modes ${A_{1g}}^1$, ${A_{1g}}^2$ and in-plane mode ${E_g}^2$ located at frequencies 71, 173 cm^{-1}, and 130 cm^{-1}, respectively, and a small peak at 37 cm^{-1}, corresponding to the ${E_g}^1$ mode, in agreement with previous characterizations of bulk samples.[47] The ${E_g}^1$ mode shows a reduced relative intensity compared to recent characterization of exfoliated flakes of 40 nm thickness previously investigated by THz s-SNOM,[48] which confirms the good quality of the MBE-grown films. While the position of the different modes is consistent in sample A and B, the intensity ratio between the out-of-plane (${A_{1g}}^1$) and the in-plane (${E_g}^2$) modes is larger in sample A, in which out-of-plane vibrations are expected to be less restrained as a consequence of the reduced crystal thickness.[49]

1.2. Magneto-Transport Experiments

Upon cooling, both samples show sheet resistances that decrease with decreasing temperature, before saturating at low temperature, implying that the electrical transport is dominated by the topologically trivial bulk states. This conclusion is supported by the low temperature magneto-transport experiments, as shown in **Figure 2**.

The sample magnetoresistance is characterized by a smooth polynomial background, indicative of ordinary magnetoresistance (Figure 2a). The Hall resistance (Figure 2b) also shows a strong non-linearity with increasing magnetic field, indicative of the presence of multiple current carriers with different mobilities.[51] When we fit this data to a two-band model, we find that there is a majority band (band 1) with high carrier density (≈10^{13} cm^{-2}) and low mobility, and a minority band (band 2) with a significantly higher mobility. The results of this fitting are summarized in **Table 1**. We assign band 1 as arising from the topologically trivial bulk states and band 2 as arising from the topologically protected surface states. We note that sample A has a significantly higher surface mobility than sample B. We ascribe this to the fact that a 1:40 Bi:Se ratio results in a much smoother surface, as shown by the Kiessig fringes in Figure 1 extending to higher angles in sample A compared to sample B. As a result,

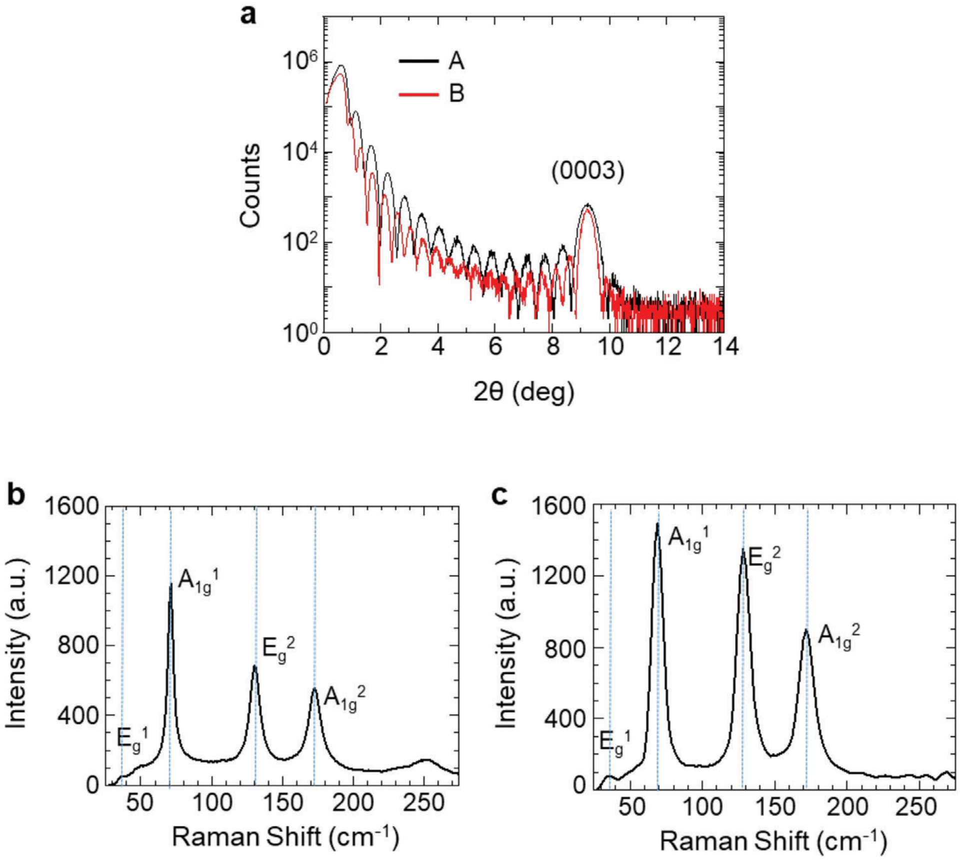

Figure 1. a) Structural characterization of the MBE-grown samples. The position of the [0003] peak is highlighted. All samples show persistent Kiessig fringes around 0 degrees and Pendellosung fringes around the [0003] peak, implying a smooth, well-ordered crystal.[50] b,c) Raman spectra of samples A (b) and B (c) after transfer onto a SiO_2/Si wafer.

scattering sites are removed from the surface, promoting surface transport.

An important signature to assess the existence of topologically protected surface states in topological insulators is the presence of Shubnikov de-Haas (SdH) oscillations in the low-temperature magnetoresistance.[52] In order to observe these oscillations, we first smooth the data with a Savitzky–Golay filter,[53] using a 3rd order polynomial before taking the 2nd derivative to remove any smoothly varying background (Figure 2c). Sample A shows clear oscillations that are periodic in inverse field, showing the Landau level quantization expected of SdH oscillations. In contrast, sample B does not show any periodicity. It is possible that due to the lower mobility of the surface states, the 8 T magnetic field employed in our experiment is not sufficient to quantize the surface states into Landau levels in sample B. The oscillations in sample A indicate a minority carrier density of 0.47×10^{13} cm^{-2}, which is consistent with the band 2 high mobility carriers shown in Table 1.

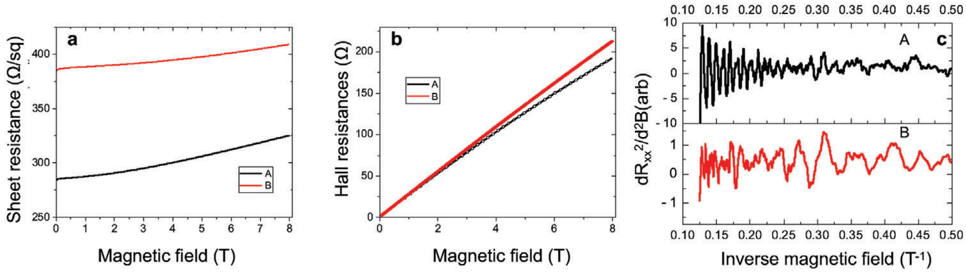

Figure 2. Summary of the low temperature magneto-transport experiments for the TI samples. a) Sheet resistance as a function of magnetic field. Note the large polynomial backgrounds present in both samples. b) Hall resistance. Both samples show a non-linear Hall response, indicative of the presence of multiple carrier species. Solid lines represent experimental data, whereas open symbols represent the fit to a two-band model performed to extract the relative carrier densities and mobilities. c) Second derivative of the longitudinal resistance as a function of the inverse magnetic field, performed to identify any oscillating component of the magnetoresistance. Sample B does not show any oscillations above the noise.

Table 1. Carrier Densities and Mobilities of the TI Samples Evaluated from Hall Experiments Fitted with the Two-Band Model.

Sample	Band 1 Carrier density [$\times 10^{13}$ cm^{-2}]	Band 1 Mobility [cm^{2}V^{-1}s^{-1}]	Band 2 Carrier density [$\times 10^{13}$ cm^{-2}]	Band 2 Mobility [cm^{2}V^{-1}s^{-1}]
A	2.5±0.2	510±50	0.55±0.05	1500±100
B	1.9±0.2	490±40	0.65±0.06	1000±100

1.3. Hyperspectral Nanoimaging Based on Near-Field Optical Holography

To shed further light on possible collective excitations arising from topologically active surface states in Bi_2Se_3, we performed THz s-SNOM on samples A and B (**Figure 3**a) to investigate the presence of TSSs. In our s-SNOM experiments, we employ a set of THz quantum cascade lasers (QCLs) operating simultaneously as source and phase-sensitive detector through the self-mixing (SFMX) effect.[54,55] This detection mechanism allows the near-field signal back-scattered from the s-SNOM to be detected as a modulation of the voltage drop on the QCL and is inherently dependent on the phase of the back-scattered field (see Figure 3a and Experimental Section). To create the near-field hologram, the relative phase between the emitted and re-injected fields is controlled with an optical delay line, which varies the optical path length *L*. In these experiments, we have employed a set of different lasers: two THz-QCL frequency combs (FCs), characterized by equally spaced modes ranging from ≈2.85 to 3.45 THz (see Figure 3b, comb I[56] and Figure S1, Supporting Information, comb II), and a sequence of single mode THz-QCLs emitting at 2.0 THz, 3.0 THz, 4.3 THz, and 4.6 THz, respectively. THz QCL FCs combine multimode emission with high spectral purity and phase coherence between the modes, which is crucial to observe a multimode self-mixing signal, as recently demonstrated both theoretically and experimentally.[57] All lasers operate in continuous wave (CW) and their emission is measured both via an under-vacuum Fourier-transform spectrometer (Vertex 80v) (Figure 3b comb I) and directly obtained from the near-field self-mixing signal (Figure 3c, comb I). Analogous data for comb II are reported in the Supporting Information. To obtain background-free near-field signals, the tip is mechanically modulated at a tapping frequency Ω (Figure 3a) and the SFMX signal is demodulated at higher harmonics *n* of the oscillation frequency, *n*Ω.

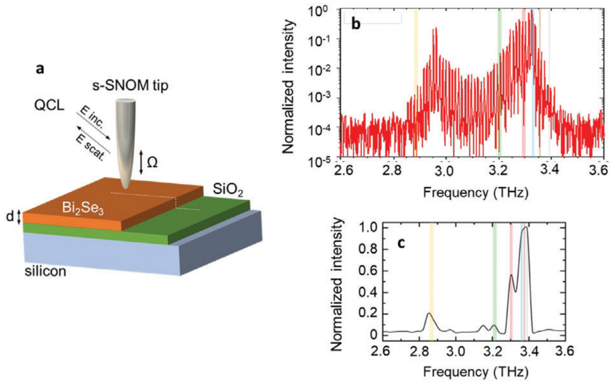

Figure 3. a) Schematic diagram showing a THz frequency comb coupled to the tip of an s-SNOM to obtain 2D near-field scattering maps at multiple frequencies. *d* is the thickness of the Bi_2Se_3 film, Ω is the tapping frequency of the s-SNOM tip. b) FTIR emission spectrum measured, under vacuum, with a 0.125 cm^{-1} resolution. c) Power spectrum of the third harmonic near-field self-mixing signal measured while sample A is illuminated with the QCL frequency comb I driven at 677 mA. The lower frequency resolution is determined by the shorter distance covered by the s-SNOM delay line, with respect to the displacement of the FTIR mirror.

The spectrum of the third harmonic near-field SFMX signal $\sigma_3 = s_3 \exp(i\phi_3)$ (Figure 3c), where s_3 is the amplitude and ϕ_3 the phase, measured on sample A while driving comb I at a current I = 677 mA, shows that despite only part of the comb modes are contributing to the self-detected near-field signal,[57] a relatively broad optical bandwidth of ≈680 GHz is spanned. Four main spectral components can be associated with the convolution of the most intense modes marked by shaded colored areas in Figure 3b. The spectrum retrieved for comb II from the 3rd order harmonic signal on the near-field maps collected on sample B also shows the presence of two main optical modes, ascribed to the spectral lines retrieved by FTIR on the same QCL (Figure S1, Supporting Information).

With this technique, we obtained hyperspectral 2D near-field maps of samples A and B. The propagation of collective excitations, such as THz polaritons, has been recently observed in Bi_2Se_3 thin films prepared by exfoliation[48] and grown by MBE[58] via s-SNOM, employing a monochromatic THz-QCL[48] and a gas laser,[58] respectively, as the pumping source. In thin MBE-grown films, polaritons have ≈12 times higher momenta compared with photons of the same energy at 3 THz.[58] Accordingly, we acquire near-field maps on the same scale of corresponding wavelength, i.e., on a 15 µm × 3 µm (sample A) and 15 µm × 2.5 µm (sample B) region including a sharp edge obtained by scratching the MBE film, in order to identify the signature of polaritons propagation (**Figure 4**a,d).

The near-field hologram is obtained by mapping the selected sample region with 300 × 500 pixels (sample A – pixel size = 50 nm × 6 nm), or 130 × 256 pixels (sample B – pixel size = 100 nm × 10 nm), and changing the optical phase at every line change along the *y*-direction by moving the delay line by ΔL = 5 µm steps. We used a non-zero scanning length along the *y*-direction to avoid mechanical instabilities, or drifts, of our s-SNOM setup. However, since the chosen region of interest is topographically invariant along the *y*-axis, the resulting holographic map represents the 1D case of the more general two-dimensional OH method.[41] Figure 4b,c,e,f show the as-obtained 3rd harmonic amplitude and phase maps for samples A (comb I) and B (comb II), respectively. The third-order near-field SFMX amplitudes in Figure 4b,e exhibit periodic oscillations induced by the phase modulation along the *y*-direction that result from the beating of the different modes that contribute to the SFMX signal of the frequency combs.

We then analyze the maps of the complex-valued $\sigma_3 = s_3 \exp(i\phi_3)$ in Fourier space to extract the s_3 and ϕ_3 maps of the third harmonics near-field signal at the different spectral components. We have followed the experimental procedure detailed in ref. [58] for extracting the polariton dispersion from the interference patterns generated by overdamped polaritonic modes in Bi_2Se_3 thin films prepared by MBE. For each spectral component, the s_3 and ϕ_3 profiles at the edge of the Bi_2Se_3 films, measured

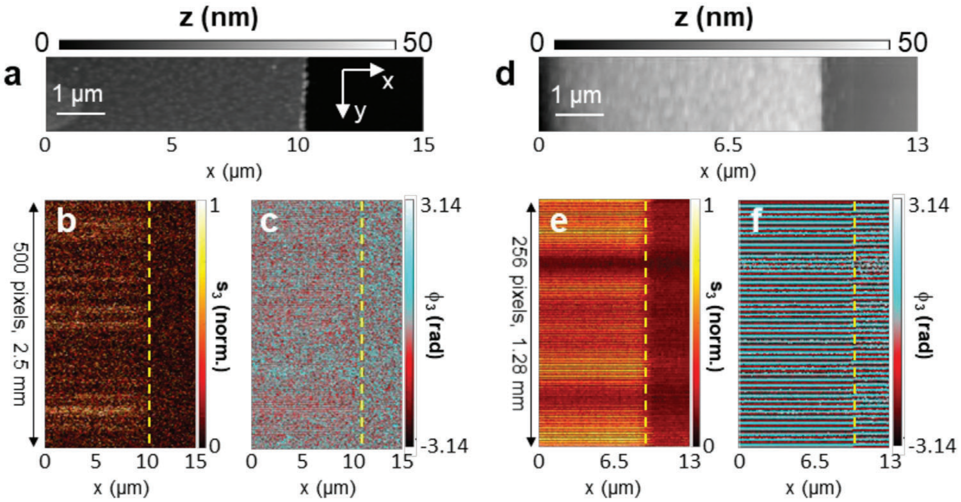

Figure 4. a,d) Topography of the SiO_2/Si-transferred Bi_2Se_3 films, sample A (a) and B (d). b,c) 300 × 500 pixels hologram acquired on sample A with the THz-QCL frequency comb I operated at 677 mA. (b) and (c) show the third-order near-field self-mixing amplitude and phase, respectively, obtained by moving the delay line by 2.5 mm. e,f) 130 × 256 pixel hologram of sample B acquired with comb II at a 796 mA driving current. (e) and (f) show the amplitude and phase, respectively, obtained by moving the delay line by 1.28 mm.

with QCL frequency combs, were extracted from the 2D maps of amplitude and phase in **Figure 5**a,b (sample A) and Figures 5e,f (sample B); see Figures 5c,d (sample A) and Figures 5g,h (sample B), respectively.

In sample B, the phase profiles exhibit a clear local maximum near the film edge, whose position shifts towards the edge for increasing photon frequency (see Figure S2, Supporting Information for further details). This effect has been previously identified as a signature of the excitation of THz plasmon polaritons in thin films of Bi_2Se_3 prepared by MBE.[58] From the amplitude and phase profiles on both samples, we evaluate the complex-valued signal σ_3 for the frequencies at which we have highest signal to noise ratio: 2.88 THz, 3.18 THz, 3.30 THz, 3.33 THz, 3.36 THz, 3.39 THz for comb I, sample A, and 3.15, 3.44 THz for comb II, sample B. The same analysis has been also performed at the frequencies of the single mode lasers employed for sample B.

We hence consider the evolution of the near-field signal σ_3 in the complex plane starting from the film-substrate interface, whose exact position is identified after analyzing the topographic maps in Figures 4a,d for samples A and B, respectively. This

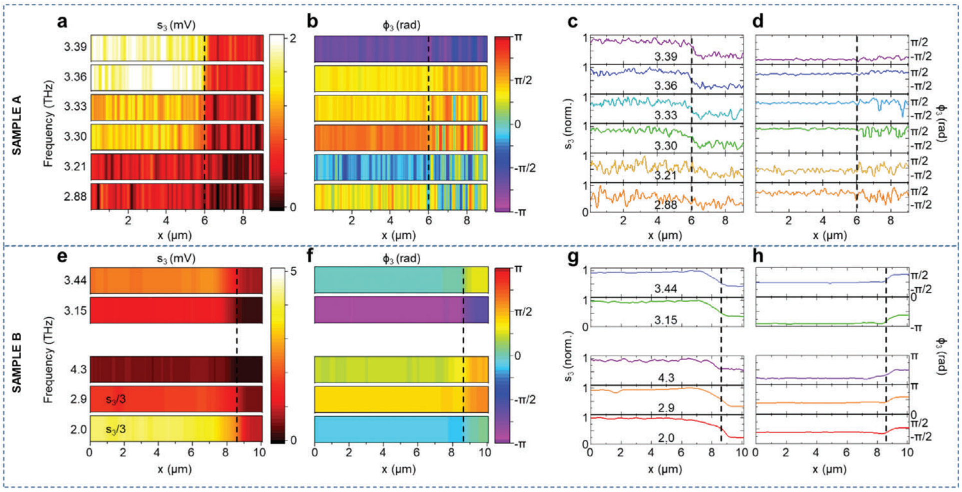

Figure 5. a,b) Extracted 2D maps of the third order near-field amplitude s_3 (a) and phase ϕ_3 (b) at the six individual frequencies marked in Figure 1 (2.88 THz, 3.18 THz, 3.30 THz, 3.33 THz, 3.36 THz, 3.39 THz), extracted from the near-field hologram in Figures 4b,c, acquired using the THz QCL frequency comb I on sample A. c,d) Linear profiles of the near-field self-mixing amplitude s_3 (c) and phase ϕ_3 (d) extracted by averaging the maps in panel a-b over the 500 vertical lines at the different frequencies. e,f) Sample B: extracted 2D maps of the third order near-field amplitude s_3 (e) and phase ϕ_3 (f) at the investigated frequencies, 3.15 and 3.44 THz for comb II, and 2.0, 2.90, and 4.30 THz for the single mode THz QCLs. Data are extracted from the near-field hologram in Figure 4e,f. g,h) Linear profiles of the near-field self-mixing amplitude s_3 (g) and phase ϕ_3 (h) extracted averaging the maps in panels e-f over the 512 vertical lines (light colored line). Dashed lines identify the Bi_2Se_3/substrate interface retrieved from the topography reported in Figure 4a,d.

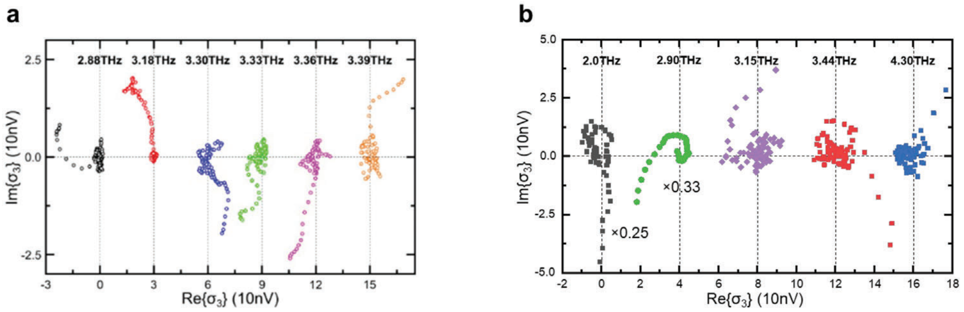

Figure 6. Determination of complex-valued polariton wavevectors. a) Complex-plane representation of σ_3 collected on sample A at 6 different frequencies with comb I. Spiral trajectories are stacked along the real axis to improve visibility. b) Complex-plane representation of the damped polaritonic oscillation occurring on sample B at different frequencies: 2 THz (single-mode source); 2.9 THz (single-mode source); 3.15 and 3.43 THz (most prominent modes of comb II); 4.3 THz (single-mode source).

procedure allows a robust determination of the polariton dispersion, including the case of overdamped modes. In polar coordinates (s_3, ϕ_3), the signal σ_3 describes spiral trajectories that correspond to damped harmonic oscillations collapsing at a complex-valued offset (**Figure 6**), which we neglect for the purpose of our analysis. Here, we analyze the spirals to extract the characteristic polariton wavelength λ_p and its damping length L_p, while fitting the curves with the function: $y = A_0 \exp(2i\mathbf{k}_p x)/\sqrt{2x}$,[58] where A_0 is a complex-valued constant, and $k_p = 2\pi/\lambda_p + i/L_p$ encodes the plasmon-polariton dynamics.

The frequency dependence of near-field contrast (**Figure 7**a,b) is quantified by dividing the average signal from the TI (a few microns away from the edge) to that of the substrate, as routinely done in nano-FTIR spectroscopy.[59] In sample A, the contrast with respect to the Si substrate, in the range 2–3.39 THz, is compatible with the values recently measured in exfoliated 16-nm-thick Bi_2Se_3 flakes in the range 2–2.7 THz,[48] but its frequency dependence well reproduces the behavior expected for hyperbolic phonon polaritons.[60] Conversely, in sample B, the contrast shows a monotonic decrease, that still agrees with the predicted 3rd order harmonic signal expected for hyperbolic phonon polaritons, but in the presence of a lower chemical potential.[60]

We use the complex-plane representation of σ_3 to obtain the polariton dispersion. The real part of the retrieved polariton wavevector $\mathrm{Re}\{k_p\}$, is shown in Figure 7b for samples A and B. The retrieved values are smaller than those observed in exfoliated TI flakes.

To understand the origin of the observed plasmon polariton (PP) oscillations quantitatively, we compare the experimental dispersion with the results obtained by an analytical conductivity model[58,61] (see Experimental Section). Here, the thin Bi_2Se_3 film is modelled as a 2D conductive layer of zero thickness, an approximation that avoids calculating the fields inside the film, and has been proven valid for in-plane isotropic[58] (and anisotropic[62]) 2D materials with layer thicknesses much smaller than the polariton wavelength.

In the model, the wavevector k_p can be expressed in terms of the total conductivity (σ_{TI}) using the relation:[63]

$$k_p = ik_0\epsilon_r \frac{c}{2\pi\sigma_{\mathrm{TI}}} \tag{1}$$

where k_0 is the free-space wavevector, ϵ_r is the average permittivity of the materials surrounding the Bi_2Se_3 layer and c is the

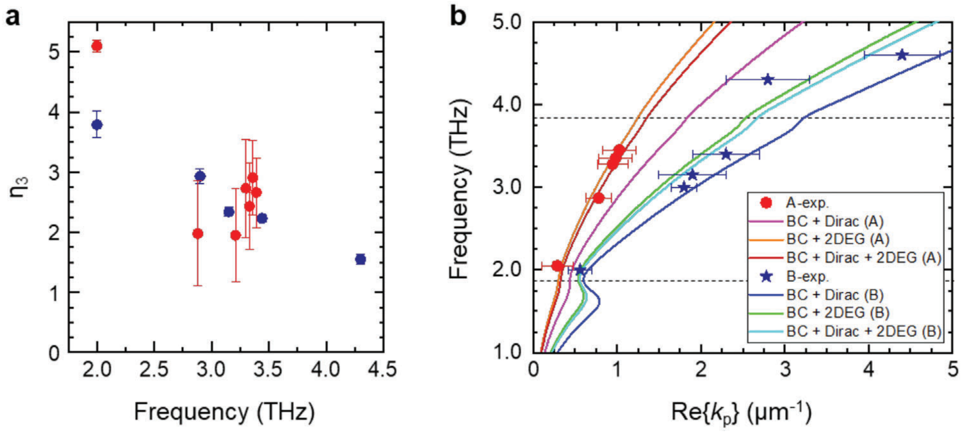

Figure 7. THz response of TI Bi_2Se_3 thin film. a) Near-field contrast between the 14.4 nm-thick (red-dots) and 19 nm-thick (blue-dots) Bi_2Se_3 films and the undoped SiO_2/Si substrate as a function of frequency. b) Polariton dispersion experimentally retrieved by polaritonic interferometry in samples A (red dots) and B (blue stars), compared with the theoretical model (lines). Error bars represent the standard deviation on the real-part of the PP wavevector as it results from the fit.

speed of light. Here, σ_{TI} is obtained by summing the bulk conductivity (σ_{bulk}) with the conductivities given by the other carrier types present in the TI layer: Dirac carriers (σ_{DC}) and massive surface carriers (σ_{2DEG}). The bulk conductivity is given by the relation $\sigma_{\mathrm{bulk}} = \epsilon_{\mathrm{bulk}} \cdot (c \cdot d/2i\lambda_0)$, where ϵ_{bulk} is the bulk permittivity, d is the film thickness and λ_0 is the free-space wavelength. Here, ϵ_{bulk} is calculated with a Drude-Lorentz model and includes the contributions of the bulk carrier density and mobility and of the transverse optical (TO) phonons $\mathrm{E_u}$ ($\omega_{\mathrm{to}}{}^{\perp} = 63.03\ \mathrm{cm^{-1}}$) and $\mathrm{A_{2u}}$ ($\omega_{\mathrm{to}}{}^{//} = 126.94\ \mathrm{cm^{-1}}$), involving atomic vibrations in the plane orthogonal (⊥) and parallel (//) to the trigonal *c*-axis, respectively.[64] The TO phonon frequencies are marked by dashed lines in Figure 7b.

By comparing the experimental data-points with the results of the analytical conductivity model, we infer that the global plasmon polaritons dispersion is given by the simultaneous contribution of bulk, Dirac and massive surface carriers to the optical conductivity, with densities given by $n_{\mathrm{bulk}} = 5.0 \times 10^{18}\ \mathrm{cm^{-3}}$, $n_{\mathrm{Dirac}} = 0.3 \times 10^{13}\ \mathrm{cm^{-2}}$, $n_{\mathrm{2DEG}} = 0.8 \times 10^{13}\ \mathrm{cm^{-2}}$ for sample A, and $n_{\mathrm{bulk}} = 8.0 \times 10^{18}\ \mathrm{cm^{-3}}$, $n_{\mathrm{Dirac}} = 0.5 \times 10^{13}\ \mathrm{cm^{-2}}$, $n_{\mathrm{2DEG}} = 0.9 \times 10^{13}\ \mathrm{cm^{-2}}$ for sample B, in reasonable agreement with the values obtained by low-temperature magneto-transport experiments. In both samples A and B, a good agreement between experiment and analytical models can be obtained only by including the contribution to the total TI conductivity of massive bulk carriers with both Dirac carriers at both $\mathrm{Bi_2Se_3}$ surfaces, and massive two-dimensional electron gases (2DEG) at both $\mathrm{Bi_2Se_3}$ surfaces (see Figure S3, Supporting Information for further details).

In conclusions, through a combination of Hall-bar magneto-transport and near-field detectorless optical holography, we have measured experimentally the dispersion of surface plasmon polariton in $\mathrm{Bi_2Se_3}$ films grown by MBE, proving the existence of massless surface carriers. Future applications of our work include the development of integrated devices for confining THz radiation to deeply subwavelength volumes, with important impacts for a new generation of nanophotonic and plasmonic devices, such as sensors, lenses or metasurfaces.

2. Experimental Section

Near-Field Nanoscopy: Indidual THz QCLs were mounted in a liquid helium continuous-flow cryostat with a high density polyethylene (HDPE) window and kept at a fixed heat sink temperature, which was laser-dependent and always set in the 10–20 K range. Temperature stability of 0.2 K was required for phase stability of the self-mixing signal. The emitted THz beam was collimated using a 90° off-axis parabolic mirror (OAP) with an effective focal length of 50 mm. The collimated THz beam was fed into the entrance optical port of a commercial near-field microscope (NeaSNOM, Neaspec/Attocube). The optical path length was varied using a delay line, equipped with two 45 deg, 2 inches plane mirrors mounted on a linear translation stage (Physik Instrumente, stepper motor stage M403.62S) having a 30 nm precision. A second OAP with an equivalent focal length of 25 mm focuses the beam onto the AFM tip of the SNOM. The laser polarization lies in the plane containing the tip to efficiently induce an oscillating dipole in the tip. THz radiation scattered by the sample was collected by the same focusing parabolic mirror and coupled back into the QCL cavity along the same incident optical path. The voltage modulation across the QCL terminals produced by the self-mixing effect was pre-amplified using a low-noise voltage amplifier (DL Instruments, mod. 1201) and demodulated up to the highest harmonic order (n = 5) allowed by the electronic board of the NeaSNOM system. The average optical path length from the QCL front facet to the tip was 70 cm.

Table 2. Parameters used in the Evaluation of the Bulk Conductivity for Sample B.

Symbol	Value [unit]/expression	Description
D	19.3 [nm]	$\mathrm{Bi_2Se_3}$ film thickness
ϵ_∞	1	permittivity at infinite frequency
ω_D	$\omega_D{}^2 = (4\pi e^2/m^*) \cdot n_{\mathrm{bulk}}$	Drude plasma frequency (CGS units)
γ_D	760 [$\mathrm{cm^{-1}}$]	Drude damping rate (electron relaxation time)
$\omega_{p,1}$	675.9 [$\mathrm{cm^{-1}}$]	TO phonon ($\mathrm{E_u}$) oscillator strength
$\omega_{0,1}$	63.03 [$\mathrm{cm^{-1}}$]	TO phonon ($\mathrm{E_u}$) center frequency
γ_1	17.5 [$\mathrm{cm^{-1}}$]	TO phonon ($\mathrm{E_u}$) damping
$\omega_{p,2}$	100 [$\mathrm{cm^{-1}}$]	TO phonon ($\mathrm{A_{2u}}$) oscillator strength
$\omega_{0,2}$	126.94 [$\mathrm{cm^{-1}}$]	TO phonon ($\mathrm{A_{2u}}$) center frequency
γ_2	10 [$\mathrm{cm^{-1}}$]	TO phonon ($\mathrm{A_{2u}}$) damping
$\omega_{p,3}$	11 249 [$\mathrm{cm^{-1}}$]	bandgap oscillator strength
$\omega_{0,3}$	2029.5 [$\mathrm{cm^{-1}}$]	Bandgap center frequency
γ_3	3920.5 [$\mathrm{cm^{-1}}$)]	Bandgap damping

Conductivity Model: In this section, we describe the analytical model employed to calculate the dispersion of plasmon polaritons in the $\mathrm{Bi_2Se_3}$ thin film, which is treated as a layer of zero thickness, characterized by an effective conductivity given by the sum of the bulk and surface contributions,[63] thus neglecting the field profile along the material thickness. This approximation was reasonable in our experiments, since the $\mathrm{Bi_2Se_3}$ thickness $d = 19$ nm is much smaller than the polariton wavelengths, which are >2 µm.

The model entails the evaluation of σ_{TI} (Equation 1), which is the total conductivity of the TI film, given by the sum of the bulk conductivity (σ_{bulk}), the massive surface carrier conductivity (σ_{2DEG}) arising from the downward bending of the conduction band at the surface[65] and the Dirac carrier conductivity (σ_{DC}). Equation 1 relates the plasmon polariton wavevector to the impinging frequency (ω) by means of the dependencies $k_0(\omega)$, $\epsilon_r(\omega)$, and $\sigma_{\mathrm{TI}}(\omega)$.

The bulk conductivity can be expressed in terms of the bulk permittivity (ϵ_{bulk}), with the expression $\sigma_{\mathrm{bulk}} = \epsilon_{\mathrm{bulk}} \cdot (c \cdot d/2i\lambda_0)$, where $\lambda_0 = 2\pi/k_0$ is the free-space wavelength. In turn, ϵ_{bulk} can be approximated by the isotropic Drude-Lorentz model described in ref. [64], and calculated by the expression:

$$\varepsilon_{\mathrm{bulk}}(\omega) = \varepsilon_\infty - \frac{\omega_{\mathrm{D}}^2}{\omega^2 + i\omega\gamma_{\mathrm{D}}} + \sum_{j=1}^{j=3} \frac{\omega_{\mathrm{p,j}}^2}{\omega_{\mathrm{0,j}}^2 - \omega^2 - i\omega\gamma_{\mathrm{j}}} \tag{2}$$

Symbols and parameters of equation 2 are explained and reported in **Table 2** (for sample B). The Drude plasma frequency is calculated as $\omega_D{}^2 = (4\pi e^2/m^*) \cdot n_{\mathrm{bulk}}$, where $m^* = 0.15\ m_e$ is the effective mass,[66] m_e the electron mass and n_{bulk} the bulk free carrier concentration.

The surface conductivity of Dirac carriers is approximated by the expression:[58]

$$\sigma_{\mathrm{DC}} = \frac{e^2 k_{\mathrm{B}} T \cdot ln\left[2\cosh\left(\frac{E_{\mathrm{F}}}{2k_{\mathrm{B}}T}\right)\right]}{2\hbar^2\pi} \cdot \frac{i}{\omega} \tag{3}$$

Where k_B is the Boltzmann constant, T is the temperature and E_{F} is the Fermi energy given by $E_{\mathrm{F}}{}^2 = (\hbar v_{\mathrm{F}})^2 \cdot 4\pi n_{\mathrm{Dirac}}$, where $\hbar$ is the reduced Plank's constant, $\nu_{\mathrm{F}} = 5 \times 10^8\ \mathrm{cm^{-1}s}$[67] and n_{Dirac} is the density of topologically protected (Dirac) surface states.

The conductivity of massive surface carriers is approximated by the expression:[58]

$$\sigma_{2\text{DEG}} = \frac{e^2 n_{2\text{DEG}}}{m^*} \cdot \frac{i}{\omega} \tag{4}$$

Where $n_{2\text{DEG}}$ is the carrier concentration.

Supporting Information

Supporting Information is available from the Wiley Online Library or from the author.

Acknowledgements

V. P., and L. V. contributed equally to this work. The authors acknowledge funding from the European Research Council through the ERC Proof of Concept Grant STAR (101081567), the FET Open project EXTREME IR (944735), the Italian Ministry of University and Research through the PNNR project PE0000023-NQSTI, and EPSRC UK programmes EP/W028921/1 and EP/P021859/1.

Conflict of Interest

The authors declare no conflict of interest.

Data Availability Statement

The data that support the findings of this study are available from the corresponding author upon reasonable request.

Keywords

Bismuth Selenide, near-field nanoscopy, terahertz, quantum cascade lasers

Received: July 12, 2023
Revised: September 8, 2023
Published online: November 7, 2023

---

[1] J. E. Moore, *Nature* **2010**, *464*, 194.
[2] M. Z. Hasan, C. L. Kane, *Rev. Mod. Phys.* **2010**, *82*, 3045.
[3] T. Zhang, P. Cheng, X. Chen, J.-F. Jia, X. Ma, K. He, L. Wang, H. Zhang, X. Dai, Z. Fang, X. Xie, Q.-K. Xue, *Phys. Rev. Lett.* **2009**, *103*, 266803.
[4] X.-L. Qi, S.-C. Zhang, *Rev. Mod. Phys.* **2011**, *83*, 1057.
[5] K. Hoefer, C. Becker, D. Rata, J. Swanson, P. Thalmeier, L. H. Tjeng, *Proc. Natl. Acad. Sci. USA* **2014**, *111*, 14979.
[6] J. He, T. M. Tritt, *Science* **2017**, *357*, eaak9997.
[7] B. Cui, A. Chen, X. Zhang, B. Fang, Z. Zeng, P. Zhang, J. Zhang, W. He, G. Yu, P. Yan, X. Han, K. L. Wang, X. Zhang, H. Wu, *Adv. Mater.* **2023**, 2302350.
[8] L. Fu, C. L. Kane, E. J. Mele, *Phys. Rev. Lett.* **2007**, *98*, 130405.
[9] L. Fu, C. L. Kane, *Phys. Rev. B* **2007**, *76*, 045302.
[10] J. C. Y. Teo, L. Fu, C. L. Kane, *Phys. Rev. B* **2008**, *78*, 045426.
[11] H. Zhang, C.-X. Liu, X.-L. Qi, X. Dai, Z. Fang, S.-C. Zhang, *Nat. Phys.* **2009**, *5*, 438.
[12] Y. Liu, W. Acuna, H. Zhang, D. Q. Ho, R. Hu, Z. Wang, A. Janotti, G. Bryant, A. V. Davydov, J. M. O. Zide, S. Law, *ACS Appl. Mater. Interfaces* **2022**, *14*, 42683.
[13] A. Politano, V. M. Silkin, I. A. Nechaev, M. S. Vitiello, L. Viti, Z. S. Aliev, M. B. Babanly, G. Chiarello, P. M. Echenique, E. V. Chulkov, *Phys. Rev. Lett.* **2015**, *115*, 216802.
[14] P. Di Pietro, M. Ortolani, O. Limaj, A. Di Gaspare, V. Giliberti, F. Giorgianni, M. Brahlek, N. Bansal, N. Koirala, S. Oh, P. Calvani, S. Lupi, *Nat. Nanotechnol.* **2013**, *8*, 556.
[15] D. Kim, P. Syers, N. P. Butch, J. Paglione, M. S. Fuhrer, *Nat. Commun.* **2013**, *4*, 2040.
[16] L. Viti, D. Coquillat, A. Politano, K. A. Kokh, Z. S. Aliev, M. B. Babanly, O. E. Tereshchenko, W. Knap, E. V. Chulkov, M. S. Vitiello, *Nano Lett.* **2016**, *16*, 80.
[17] Y. Wang, S. V. Mambakkam, Y.-X. Huang, Y. Wang, Y. Ji, C. Xiao, S. A. Yang, S. A. Law, J. Q. Xiao, *Phys. Rev. B* **2022**, *106*, 155408.
[18] Z. Wang, S. Law, *Cryst. Growth Des.* **2021**, *21*, 6752.
[19] K. Kondou, R. Yoshimi, A. Tsukazaki, Y. Fukuma, J. Matsuno, K. S. Takahashi, M. Kawasaki, Y. Tokura, Y. Otani, *Nat. Phys.* **2016**, *12*, 1027.
[20] O. Chiatti, C. Riha, D. Lawrenz, M. Busch, S. Dusari, J. Sánchez-Barriga, A. Mogilatenko, L. V. Yashina, S. Valencia, A. A. Ünal, O. Rader, S. F. Fischer, *Sci. Reports* **2016**, *6*, 27483.
[21] R. Giraud, J. Dufouleur, *Phys. status solidi* **2021**, *258*, 2000066.
[22] B. Lv, T. Qian, H. Ding, *Nat. Rev. Phys.* **2019**, *1*, 609.
[23] L. Locatelli, A. Kumar, P. Tsipas, A. Dimoulas, E. Longo, R. Mantovan, *Sci. Rep.* **2022**, *12*, 3891.
[24] T. Zhang, N. Levy, J. Ha, Y. Kuk, J. A. Stroscio, *Phys. Rev. B* **2013**, *87*, 115410.
[25] M. Chen, J.-P. Peng, H.-M. Zhang, L.-L. Wang, K. He, X.-C. Ma, Q.-K. Xue, *Appl. Phys. Lett.* **2012**, *101*, 081603.
[26] P. Di Pietro, F. M. Vitucci, D. Nicoletti, L. Baldassarre, P. Calvani, R. Cava, Y. S. Hor, U. Schade, S. Lupi, *Phys. Rev. B.* **2012**, *86*, 045439.
[27] W. Witczak-Krempa, J. Maciejko, *Phys. Rev. Lett.* **2016**, *116*, 100402.
[28] D. Hsieh, Y. Xia, D. Qian, L. Wray, J. H. Dil, F. Meier, J. Osterwalder, L. Patthey, J. G. Checkelsky, N. P. Ong, A. V. Fedorov, H. Lin, A. Bansil, D. Grauer, Y. S. Hor, R. J. Cava, M. Z. Hasan, *Nature* **2009**, *460*, 1101.
[29] C. Jürß, D. Bauer, *Phys. Rev. B* **2022**, *106*, 054303.
[30] L. Braun, G. Mussler, A. Hruban, M. Konczykowski, T. Schumann, M. Wolf, M. Münzenberg, L. Perfetti, T. Kampfrath, *Nat. Commun.* **2016**, *7*, 13259.
[31] Y. Zhang, *IOP Conf. Ser.: Mater. Sci. Eng.* **2019**, *563*, 022033.
[32] M. S. Claro, I. Levy, A. Gangopadhyay, D. J. Smith, M. C. Tamargo, *Sci. Rep.* **2019**, *9*, 3370.
[33] P. W. Bridgman, *Proc. Am. Acad. Arts Sci* **1925**, *60*, 305.
[34] D. C. Stockbarger, *Rev. Sci. Instrum.* **1936**, *7*, 133.
[35] S. Y. F. Zhao, C. Beekman, L. J. Sandilands, J. E. J. Bashucky, D. Kwok, N. Lee, A. D. Laforge, S. W. Cheong, K. S. Burch, *Appl. Phys. Lett.* **2011**, *98*, 141911.
[36] H. Cui, H. Liu, J. Wang, X. Li, F. Han, R. I. Boughton, *J. Cryst. Growth* **2004**, *271*, 456.
[37] Y.-F. Lin, H.-W. Chang, S.-Y. Lu, C. W. Liu, *J. Phys. Chem. C* **2007**, *111*, 18538.
[38] H. Tang, D. Liang, R. L. J. Qiu, X. P. A. Gao, *ACS Nano* **2011**, *5*, 7510.
[39] X. Chen, X.-C. Ma, K. He, J.-F. Jia, Q.-K. Xue, *Adv. Mater.* **2011**, *23*, 1162.
[40] Y. Li, J. W. Bowers, J. A. Hlevyack, M.-K. Lin, T.-C. Chiang, *ACS Nano* **2022**, *16*, 9953.
[41] M. Schnell, P. S. Carney, R. Hillenbrand, *Nat. Commun.* **2014**, *5*, 3499.
[42] C. S. Knox, M. T. Vaughan, A. D. Burnett, M. Ali, S. Sasaki, E. H. Linfield, A. G. Davies, J. R. Freeman, *Phys. Rev. B* **2022**, *106*, 245203.
[43] N. Kato, A. R. Lang, *Acta Cryst* **1959**, *12*, 787.
[44] S. Nakajima, *J. Phys. Chem. Solids* **1963**, *24*, 479.
[45] A. Majumdar, *Science* **2004**, *303*, 777.
[46] J. Zhang, Z. Peng, A. Soni, Y. Zhao, Y. Xiong, B. Peng, J. Wang, M. S. Dresselhaus, Q. Xiong, *Nano Lett.* **2011**, *11*, 2407.

[47] W. Richter, C. R. Becker, *Phys. Status Solidi B* **1977**, *84*, 619.

[48] E. A. A. Pogna, L. Viti, A. Politano, M. Brambilla, G. Scamarcio, M. S. Vitiello, *Nat. Commun.* **2021**, *12*, 6672.

[49] K. M. F. Shahil, M. Z. Hossain, V. Goyal, A. A. Balandin, *J. Appl. Phys.* **2012**, *111*, 054305.

[50] E. S. Walker, S. R. Na, D. Jung, S. D. March, J.-S. Kim, T. Trivedi, W. Li, L. Tao, M. L. Lee, K. M. Liechti, D. Akinwande, S. R. Bank, *Nano Lett.* **2016**, *16*, 6931.

[51] H. H. Wieder, *Appl. Phys. Lett.* **1974**, *25*, 206.

[52] W. Zhao, L. Chen, Z. Yue, Z. Li, D. Cortie, M. Fuhrer, X. Wang, *npj Quantum Mater.* **2019**, *4*, 56.

[53] W. H. Press, S. A. Teukolsky, *Computers in Physics and IEEE Computational Science & Engineering* **1990**, *4*, 669.

[54] M. C. Giordano, S. Mastel, C. Liewald, L. L. Columbo, M. Brambilla, L. Viti, A. Politano, K. Zhang, L. Li, A. G. Davies, E. H. Linfield, R. Hillenbrand, F. Keilmann, G. Scamarcio, M. S. Vitiello, *Opt. Express* **2018**, *26*, 18423.

[55] E. A. A. Pogna, C. Silvestri, L. L. Columbo, M. Brambilla, G. Scamarcio, M. S. Vitiello, *APL Photonics* **2021**, *6*, 061302.

[56] E. Riccardi, V. Pistore, L. Consolino, A. Sorgi, F. Cappelli, R. Eramo, P. De Natale, L. Li, A. G. Davies, E. H. Linfield, M. S. Vitiello, *Laser Photonics Rev.* **2023**, *17*, 2200412.

[57] V. Pistore, E. A. A. Pogna, L. Viti, L. Li, A. G. Davies, E. H. Linfield, M. S. Vitiello, *Adv. Sci.* **2022**, *9*, 2200410.

[58] S. Chen, A. Bylinkin, Z. Wang, M. Schnell, G. Chandan, P. Li, A. Y. Nikitin, S. Law, R. Hillenbrand, *Nat. Commun.* **2022**, *13*, 1374.

[59] A. Cvitkovic, N. Ocelic, R. Hillenbrand, *Opt. Express* **2007**, *15*, 8550.

[60] J.-S. Wu, D. N. Basov, M. M. Fogler, *Phys. Rev. B* **2015**, *92*, 205430.

[61] F. J. Alfaro-Mozaz, S. G. Rodrigo, P. Alonso-González, S. Vélez, I. Dolado, F. Casanova, L. E. Hueso, L. Martín-Moreno, R. Hillenbrand, A. Y. Nikitin, *Nat. Commun.* **2019**, *10*, 42.

[62] S. Chen, P. L. Leng, A. Konečná, E. Modin, M. Gutierrez-Amigo, E. Vicentini, B. Martín-García, M. Barra-Burillo, I. Niehues, C. Maciel Escudero, X. Y. Xie, L. E. Hueso, E. Artacho, J. Aizpurua, I. Errea, M. G. Vergniory, A. Chuvilin, F. X. Xiu, R. Hillenbrand, *Nat. Mater.* **2023**, *8*, 1374.

[63] A. Y. Nikitin, in *World Scientific Handbook of Metamaterials and Plasmonics. Recent Progress in the Field of Nanoplasmonics*, 4, (Ed.: J. Aizpurua), World Scientific, **2017**.

[64] Y. Deshko, L. Krusin-Elbaum, V. Menon, A. Khanikaev, J. Trevino, *Opt. Express* **2016**, *24*, 7398.

[65] M. Bianchi, D. Guan, S. Bao, J. Mi, B. B. Iversen, P. D. C. King, P. Hofmann, *Nat. Commun.* **2010**, *1*, 128.

[66] N. Bansal, Y. S. Kim, M. Brahlek, E. Edrey, S. Oh, *Phys. Rev. Lett.* **2012**, *109*, 116804.

[67] A. A. Reijnders, Y. Tian, L. J. Sandilands, G. Pohl, I. D. Kivlichan, S. Y. F. Zhao, S. Jia, M. E. Charles, R. J. Cava, N. Alidoust, S. Xu, M. Neupane, M. Z. Hasan, X. Wang, S. W. Cheong, K. S. Burch, *Phys. Rev. B.* **2014**, *89*, 075138.